Acta Pharmaceutica Sinica B 2026;16(3):1662−1675

Chinese Pharmaceutical Association
Institute of Materia Medica, Chinese Academy of Medical Sciences

Acta Pharmaceutica Sinica B

www.elsevier.com/locate/apsb
www.sciencedirect.com

ORIGINAL ARTICLE

Heterocyclic modified paclitaxel prodrug nanoassemblies for stimuli-responsive delivery *via* lysosomal escape

Mingyang Han[a,†], Hezhen Xu[a,†], Jun Yuan[a], Wenxiao Li[a], Hao Zhang[a], Hongkai Fang[a], Zhiyu Kuang[a], Yuanhao Yu[a], Danping Wang[a], Zhenzhen Zhao[c], Cong Luo[a,b,*], Bingjun Sun[a,b,*], Jin Sun[a,b,*]

[a]*Wuya College of Innovation, Shenyang Pharmaceutical University, Shenyang 110016, China*
[b]*Joint International Research Laboratory of Intelligent Drug Delivery Systems, Ministry of Education, Shenyang Pharmaceutical University, Shenyang 110016, China*
[c]*Department of Pharmacy, The First Affiliated Hospital of Jinzhou Medical University, Jinzhou 121000, China*

Received 23 May 2025; received in revised form 1 July 2025; accepted 7 July 2025

KEY WORDS

Heterocyclic tertiary amine;
Lysosomal escape;
Proton sponge effect;
Paclitaxel prodrug nanoassemblies;
Modular design;
Stimuli-responsive;
Drug delivery;
Cancer therapy

Abstract Prodrug nanoassemblies offer an innovative approach to drug delivery, but their lysosomal entrapment often impairs drug release. Notably, tertiary amine structures can undergo protonation reactions, thereby facilitating lysosomal escape through the proton sponge effect. In this study, we developed three novel paclitaxel prodrug nanoassemblies (PTX−SS−NO NPs, PTX−SS−CC NPs and PTX−SS−NC NPs) featuring distinct heterocyclic tertiary amine structures to investigate structure-activity relationships in lysosomal escape and drug delivery. Among them, PTX−SS−NC NPs demonstrated excellent lysosomal escape capability, enabling rapid drug release into the cytosol. Systematic evaluation revealed that the PTX−SS−NC NPs exhibited optimized pharmacokinetics and significant tumor accumulation, further contributing to their strong antitumor efficacy. Our findings establish heterocyclic tertiary amines as crucial design elements for overcoming lysosomal entrapment and optimizing chemotherapeutic prodrug nanoassemblies.

*Corresponding authors.
E-mail addresses: luocong@syphu.edu.cn (Cong Luo), sunbingjun_spy@sina.com (Bingjun Sun), sunjin@syphu.edu.cn (Jin Sun).
[†]These authors made equal contributions to this work.
Peer review under the responsibility of Chinese Pharmaceutical Association and Institute of Materia Medica, Chinese Academy of Medical Sciences.

https://doi.org/10.1016/j.apsb.2026.01.017

1. Introduction

Chemotherapy holds an indispensable position in cancer treatment[1]. However, most chemotherapeutic drugs suffer from low delivery efficiency and high systemic toxicity, which limit their clinical application[2]. Paclitaxel (PTX) is a widely used drug for treating various malignancies, including breast cancer, non-small cell lung cancer, and ovarian cancer[3]. The poor solubility of PTX necessitates the usage of the polyoxyethylene castor oil in its commercial injectable formulation, Taxol®[4,5]. Unfortunately, the surfactants can lead to hypersensitivity reactions and peripheral neuropathy, further complicating their clinical application[6]. These issues underscore the need for innovative delivery systems to enhance the efficacy and safety of PTX.

Nanodrug delivery systems have experienced rapid developments, with distinct advantages including prolonged circulation time, improved tumor accumulation, and controlled drug release[7−10]. Prodrug nanoassemblies offer an innovative strategy for drug delivery through the self-assembly of prodrugs[11]. Unlike traditional carrier-dependent systems such as liposomes and micelles, prodrug nanoassemblies do not require additional carrier materials[12]. Instead, the prodrugs function as both carriers and therapeutic agents, offering several advantages such as high drug loading (>50%) and low excipient-related toxicity[13,14]. Generally, prodrug nanoassemblies consist of three essential modules: the drug module, the response module, and the modification module[15]. The drug module contains the active pharmaceutical ingredient that exerts the therapeutic effect upon release[16]. The modification module can drive the self-assembly process through balancing intermolecular forces, such as the alkyl chain containing branched chains, straight chains, or cyclic chains[17,18]. The response module guarantees the specific release of the drug at the tumor site[19]. For example, the disulfide bond as an effective response module possesses unique redox properties to respond to the elevated levels of reactive oxygen species (ROS) and glutathione (GSH) in the tumor[20,21]. As a result, the prodrugs can release active components specifically within tumor tissues, minimizing exposure to normal cells and reducing the side effects.

Like many nanomedicines, prodrug nanoassemblies enter tumor cells primarily through endocytosis and are subsequently transported to lysosomes[22,23]. The acidic environment and the abundance of hydrolases in lysosomes often lead to the degradation of nanoassemblies, preventing them from exerting therapeutic effects[24]. Therefore, it is crucial for nanoassemblies to escape from lysosomes efficiently to ensure that the drugs can be released at the desired site of action. To address lysosomal entrapment, the proton sponge effect is developed as a promising strategy[25]. This mechanism leads to lysosomal swelling and rupture, a process that typically necessitates the presence of amino groups for its occurrence. Nitrogen has a lone pair of electrons that can accept the protons and then trigger the proton sponge effect[26,27]. Therefore, it is reasonable to hypothesize that the introduction of amino groups into the modification module would facilitate the lysosomal escape of prodrug nanoassemblies. At the same time, other atoms on the modification module may also have an important effect on the lysosome escape and drug release of prodrug nanoassemblies[28]. Based on this hypothesis, we designed piperidino and morpholino as modification modules. Meanwhile, cyclohexyl was introduced as a modification module as the control form for exploring the structure of cyclic tertiary amines. Therefore, a deeper understanding of how these factors affect the lysosomal escape capability needs to be further explored. It is expected to provide some basis for the subsequent research on prodrugs with heterocyclic tertiary amine structures and the delivery strategies of lysosome escape.

Herein, we reported smart stimuli-responsive heterocyclic tertiary amine−PTX prodrug nanoassemblies (HTAPs) for efficient cancer therapy[29]. As shown in Fig. 1, morpholino, cyclohexyl, and piperidino were used as modification modules to conjugate with PTX *via* disulfide bonds. The corresponding prodrug nanoassemblies were PTX−SS−NO NPs, PTX−SS−CC NPs and PTX−SS−NC NPs, named based on the difference in the ring structure. We explored the role of the heterocyclic tertiary amine in the construction of HTAPs. The difference in heteroatoms contributed to varying self-assembly stability, which in turn affected the rate of stimulus-responsive drug release. Simultaneously, we evaluated the transformations of HTAPs under highly acidic conditions, and the mechanism of lysosomal escape was also investigated. Moreover, we compared the differences in antitumor effects among HTAPs. Although PTX−SS−NO NPs had the best assembly stability and high cellular uptake due to positive charge, they had the worst antitumor efficacy due to the slow drug release rate, lysosomal entrapment, and rapid clearance *in vivo*. Interestingly, PTX−SS−NC NPs exhibited strong antitumor efficacy driven by excellent lysosomal escape ability, efficient tumor accumulation, and rapid drug release. Remarkably, even at a high dose of 40 mg/kg, no adverse effects were observed in mice. This study illustrated the crucial role of heterocyclic tertiary amine as the modification module for enhancing both efficacy and safety.

2. Materials and methods

2.1. Materials

N-(Carbonyl-methoxy polyethylene glycol 2000)-1,2-distearoyl-*sn*-glycerol-3-phosphoethanolamine (DSPE-PEG_{2k}) was obtained from AVT (Shanghai) Pharmaceutical Tech Co., Ltd. (Shanghai, China). DiR, paclitaxel (PTX, 99.0%), docetaxel (99.0%), glutathione (GSH, 98.0%), Hoechst 33342 and 3-(4,5-dimethylthiazol-2-yl)-2,5-diphenyltetrazolium bromide (MTT, 98.0%), tissue fixative, fetal bovine serum (FBS) and all cell media were purchased from Dalian Meilun Biotechnology Co., Ltd. (Dalian, China). Hydrogen peroxide (H_2O_2, 30%) and coumarin-6 (98.0%) were supplied by Shanghai Aladdin Biochemical Technology Co., Ltd. (Shanghai, China). *N*-(3-Aminopropyl) morpholine (98.0%), 1-(3-aminopropyl) piperidine (98.0%), 3-cyclohexylpropylamine (97.0%), 4,4′-dithiodibutyric acid (99.0%), dimethyl sulfoxide (DMSO, 99.0%), 4-dimethylaminopyridine (DMAP, 99.0%), *N*-(3-dimethylaminopropyl)-*N*′-ethylcarbodiimidehydrochloride

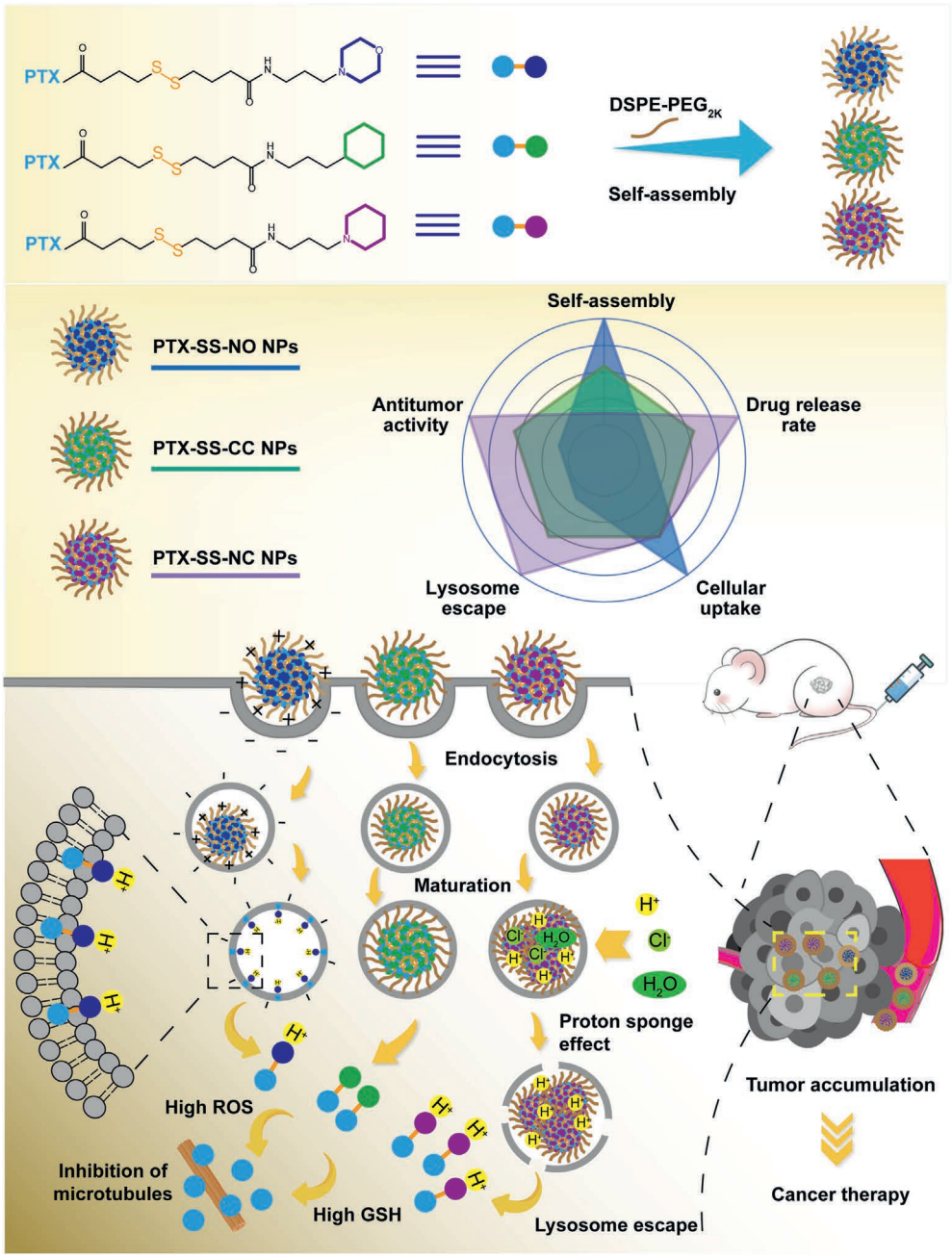

Figure 1 Heterocyclic tertiary amine−PTX prodrug nanoassemblies (HTAPs) for efficient cancer therapy.

(EDCI, 99.0%), *N*,*N*-diisopropylethylamine (DIPEA, 99.0%), 2-(7-azabenzotriazol-1-yl)-*N*,*N*,*N*′,*N*′-tetramethyluronium hexafluorophosphate (HATU, 99.0%) and 2-(1*H*-benzotriazole-1-yl)-1,1,3,3-tetramethyluronium hexafluorophosphate (HBTU, 99.0%) was obtained from Shanghai Macklin Biochemical Co., Ltd. (Shanghai, China). The 96-well plate, 24-well plate, 12-well plate, and 6-well plate were purchased from NEST Biotechnology (Wuxi, China).

2.2. *Synthesis of HTAP*

Synthesis of PTX−SS: 4,4′-dithiodibutyric acid (1.428 g, 6.0 mmol) was added to a round-bottom flask and dissolved in dichloromethane (DCM). EDCI (573.0 mg, 3.0 mmol) dissolved in DCM was added dropwise to 4,4′ -dithiodibutyric acid at 4 °C with stirring for 0.5 h. PTX (1.281 g, 1.5 mmol) and DMAP (146.4 mg, 1.2 mmol) were dissolved in DCM, respectively. Then, PTX and DMAP were added dropwise to the above system and reacted under the protection of nitrogen at room temperature for 24 h. Finally, the crude products were purified by reverse-phase preparative high-performance liquid chromatography. PTX−SS was isolated with 70% ACN/H_2O (49% yield).

Synthesis of PTX−SS−NO: First, PTX−SS (107.3 mg, 0.1 mmol) and HATU (76.1 mg, 0.2 mmol) were dissolved in DCM, respectively, under an ice bath for 10 min. Subsequently, DIPEA was added dropwise to the reaction mixture, which was stirred for 1 h. Following this, *N*-(3-aminopropyl) morpholine (15.0 μL) was added dropwise into the whole system at room

temperature for 24 h under a nitrogen atmosphere. Finally, the crude products were purified by reverse-phase preparative high-performance liquid chromatography. PTX−SS−NO was isolated with 100% ACN/H_2O (31% yield).

Synthesis of PTX−SS−CC: PTX−SS (107.3 mg, 0.1 mmol) and HBTU (75.8 mg, 0.2 mmol) were dissolved in DCM and stirred in an ice bath for 10 min. Then DIPEA was slowly dropped into the above system and kept stirring for 1 h. Approximately 15 μL of 3-cyclohexylpropylamine was slowly added to the above system. The reaction was conducted under a nitrogen atmosphere at room temperature for 24 h. Finally, the crude products were purified by reverse-phase preparative high-performance liquid chromatography. PTX−SS−CC was isolated with 80% ACN/H_2O (25% yield).

Synthesis of PTX−SS−NC: PTX−SS (107.3 mg, 0.1 mmol) and HBTU (76.1 mg, 0.2 mmol) were dissolved in DCM, respectively, under an ice bath for 10 min. 25 mL of triethylamine was added dropwise to the above system. 1-(3-Aminopropyl) piperidine (15.0 μL) was added dropwise into the whole system at room temperature for 24 h under a nitrogen atmosphere. Finally, the crude products were purified by reverse-phase preparative high-performance liquid chromatography. PTX−SS−NC was isolated with 65% ACN/H_2O (7% yield).

Confirmation: Mass spectrometer (FT-MS, Bruker) and nuclear magnetic resonance spectroscopy (600 MHz ^{1}H NMR, Bruker AV-400) were applied to determine the prodrug structures.

2.3. Preparation and characterization of prodrug nanoassemblies

Prodrug nanoassemblies were prepared by a one-step nano-precipitation method. Briefly, the prodrug solution with the corresponding concentration was prepared with anhydrous ethanol, which was added to the deionized water and stirred, and the non-PEGylated nanoassemblies with different concentrations were separately prepared. Next, a mixture of heterocyclic tertiary amine−PTX prodrugs (HTAP) and DSPE-PEG_{2k} with the corresponding concentration (4:1) is prepared with anhydrous ethanol and then added to the deionized water under stirring. Subsequently, the ethanol was removed under reduced pressure to obtain heterocyclic tertiary amine−PTX prodrug nanoassemblies (HTAPs, 1 mg/mL). Similarly, fluorescent dye-labeled HTAPs were prepared by adding coumarin-6 or DiR into the organic phase.

The nanoassemblies were diluted to 50 μg/mL. Particle size, PDI, and zeta potential of prodrug nanoassemblies were measured by the Zetasizer instrument (Nano ZS, Malvern Co., UK). Transmission electron microscopy (TEM) was used to observe the nanoassemblies' morphology.

The drug loading capacity of HTAPs was calculated according to the following Eq. (1), that is, the PTX content in each preparation:

$$\text{Drug loading}\ (\%) = \frac{\frac{m_m}{M} \times M_{PTX}}{m_m + m_p} \times 100\% \quad (1)$$

Where m_m represents the mass of the prodrug, M represents the molecular weight of the prodrug, M_{PTX} represents the molecular weight of PTX, and m_p represents the mass of DSPE-PEG_{2k}.

2.4. Molecular docking

The molecular docking evaluation of HTAP was carried out using the Yinfo Cloud Computing Platform, and the specific operations were as follows: the compound structure was prepared by selecting a gadget, and the calculation method of creating a project was selected to select the small molecule-small molecule docking (DOCK 6.9) mode. The molecular structure selects the same file (both as a host molecule and as a guest molecule). The receptor binding site was defined as the docking pocket, and the (grid) box was set to fully encompass the molecular structure. Flexible ligand docking was selected as the calculation mode.

2.5. Stability assessment

1 mL of HTAPs was diluted in 10 mL PBS (pH 7.4, containing 10% FBS). The mixtures were incubated at 37 °C in a shaker (100 rpm, Honour, OE-1, Tianjin, China). The colloidal stability of HTAPs was examined by measuring the particle size using a Zetasizer instrument (Nano ZS, Malvern Co., UK) at predetermined intervals (0, 2, 4, 6, 8, 12 and 24 h). As for long-term storage stability, HTAPs were stored at 4 °C for up to 30 days, and then the particle size of each group was measured on the indicated day. The size changes of HTAPs stored at room temperature for 30 days were also evaluated.

2.6. Change pH

Potential changes of HTAPs at pH 7.4, 5.0 and 4.5, respectively. Then they were placed at pH 4.5 for 12 h to observe the changes in HTAPs and measure the particle size.

2.7. In vitro drug release

PBS containing 30% anhydrous ethanol (*v/v*) was used as the release medium. The release medium was prepared with or without the addition of H_2O_2 at concentrations of 1, 5, and 10 mmol/L, or GSH at concentrations of 0.05 and 0.5 mmol/L. The release of PBS (pH 5.0) with 30% anhydrous ethanol as the release medium was also tested. Briefly, HTAPs (400 μL, 500 μmol/L) were added to 30 mL of the above medium and oscillated in a 37 °C air bath shaker. After that, samples were taken at prescriptive intervals, and the concentration of released PTX in the system was quantified at a wavelength of 227 nm by high-performance liquid chromatography (HPLC, Hitachi, Japan). The data are presented as the mean ± standard deviation (SD) ($n = 3$).

2.8. Cell lines

All the cell lines mentioned (4T1 cells, B16-F10 cells, A549 cells, 3T3 cells) in this study were provided by the cell bank of the Type Culture Collection of the Chinese Academy of Sciences (Beijing, China). All culture media (RPMI-1640, DMEM, DMEM-F12) were supplemented with 10% (*v/v*) FBS, streptomycin sulphate and penicillin (100 units/mL and 100 μg/mL, respectively). The cells were grown in a cell incubator, maintained at 37 °C and 5% CO_2.

2.9. Cellular uptake

In brief, 4T1 cells were seeded in 24-well plates with pre-placed covered slides (5×10^4 cells per well) and incubated for 24 h. Then, fresh medium containing free coumarin-6 or coumarin-6-labeled HTAPs (equivalent to 250 ng/mL coumarin-6) was added and further incubated for 0.5, 2 and 4 h. After that, the cells

were gently washed with cold PBS. Subsequently, a tissue fixative was utilized to fix the cells. Following fixation, the cells were washed again and counterstained with Hoechst 33342. Finally, the cell uptake behavior was visualized by confocal laser scanning microscopy (CLSM, TCS SP2/AOBS, LEICA, Germany). For quantitative analysis of cellular uptake, flow cytometry was applied to measure the fluorescence intensity within cells.

Cellular uptake was quantified using UPLC−MS/MS (Waters Co., Ltd., Milford, MA, USA). 4T1 cells were seeded in 6-well plates (3×10^5 cells per well) and incubated for 24 h. Then, fresh medium containing Taxol, Abraxane or HTAPs (equivalent to 5 μg/mL PTX) was added and further incubated for 0.5, 2 and 4 h. After that, the cells were gently washed with cold PBS. 500 μL deionized water was added to each well, then all cells were scraped off and collected into 1.5 mL EP tubes. The cells were treated with an ultrasonic crusher. Finally, the intracellular drug concentration was determined with the BCA protein quantification/concentration assay kit.

2.10. Cytotoxicity assays

Typically, 4T1, B16-F10, A549 and L02 cells were seeded in 96-well plates (4T1 and B16-F10 cells: 2×10^3 cells per well, A549 cells: 3×10^3 cells per well, L02 cells: 1×10^4 cells per well) and incubated for 18−24 h. After removing the old medium, the cells were exposed to fresh medium containing serial concentrations of Taxol, HTAPs or HTAP aq (the solution of HTAP), followed by culturing for 48 h. Finally, cell viability was then determined using the MTT assay. The IC_{50} values were calculated by GraphPad Prism 9.5.1 software ($n = 3$).

The preparation conditions of HTAP aq were as follows: HTAP was initially dissolved in DMSO to obtain a stock solution at a concentration of 5 mg/mL. Then the stock solution was diluted with cell culture medium to ensure that the final concentration of DMSO did not exceed 0.1% (*v*/*v*). The cell variability is calculated as following Eq. (2):

$$\text{Cell viability}\ (\%) = \frac{A_s - A_b}{A_c - A_b} \times 100\% \quad (2)$$

Where A_s represents the absorbance of the sample group, A_b represents the absorbance of the blank group, and A_c represents the absorbance of the control group. The selectivity index is calculated as following Eq. (3):

$$SI = \frac{IC_{50}}{IC_{50d}} \quad (3)$$

Where IC_{50} represents the half maximum inhibitory concentration of each type of tumor cells, and IC_{50d} represents the half maximum inhibitory concentration of 3T3 cells.

2.11. Intracellular drug release

In brief, 4T1 cells were seeded in 24-well plates at a density of 1×10^5 cells per well. After 24 h incubation, the cells were treated with Taxol, Abraxane and HTAPs at concentrations of 100, 200 and 500 ng/mL corresponding to the PTX content. The cells were further incubated for 48 h. After that, the cells and the culture medium were collected for analysis of the concentrations of free PTX using UPLC−MS/MS[30].

2.12. Lysosomal colocalization assay

Glass-bottom culture dishes were selected, and 1 mL of 4T1 cell suspension (1×10^5 cells/mL) was inoculated into each small dish and cultured in the cell incubator for 24 h. Then, fresh medium containing free coumarin-6 or coumarin-6-labeled HTAPs (equivalent to 250 ng/mL coumarin-6) was added and further incubated for 2, 4 and 8 h. After that, the cells were gently washed with cold PBS. DND-99 was used sequentially and stained with Hoechst 33342 according to the kit instructions, respectively. Finally, the lysosomal colocalization was observed by CLSM and the Pearson correlation coefficient was calculated.

2.13. Hemolysis assay

Blood was collected from the orbital vein of healthy rats and centrifuged at 14,465×*g* for 10 min. Then the 2% (*v*/*v*) red blood cell suspension was prepared using PBS. Subsequently, the blood cell suspension was mixed with PBS, Triton X-100 and prodrug nanoassemblies, and placed in the shaker (37 °C, Honour) for 1 h. After 10 min of centrifugation at 14,465×*g*, the supernatant was collected to measure the absorbance. Percentage of hemolysis (%) was calculated as following Eq. (4):

$$\text{Percentage of hemolysis}\ (\%) = \frac{A_y - A_n}{A_p - A_n} \times 100\% \quad (4)$$

Where A_y represents the test sample, A_n represents the negative control (Samples treated with PBS), and A_p represents the positive control (Samples treated with Triton X-100).

2.14. Animals

All the animals were provided by the Laboratory Animal Center of Shenyang Pharmaceutical University (Shenyang, China). All experiments involving live animals were performed in strict accordance with the animal experimentation guidelines and were approved by the Institutional Animal Ethical Care Committee (IAEC) of Shenyang Pharmaceutical University.

2.15. Pharmacokinetic study in vivo

A pharmacokinetic study on male Sprague−Dawley rats was performed to the obtain plasma concentration-time profile of HTAPs. The rats were randomly assigned to different groups ($n = 5$ for each group) and intravenously administered Taxol, Abraxane or HTAPs (equivalent to 6 mg/kg of PTX). At predetermined time points, the blood samples were collected and centrifuged to obtain plasma. Afterwards, proteins were precipitated to extract the analytes from plasma. Docetaxel was used as an internal standard. The concentrations of prodrugs and PTX were quantified by UPLC−MS/MS. Chromatographic conditions: Phenomenex Kinetex XB-C18 column (50 mm × 2.1 mm, 2.6 μm); mobile phase acetonitrile and water (95/5, *v*/*v*) with 0.1% (*v*/*v*) ammonia solution; flow rate 0.2 mL/min, injection volume 5 μL. The pharmacokinetic parameters, including AUC, $t_{1/2}$, and C_{max} were calculated by DAS 2.0 software.

2.16. Biodistribution

To study the biodistribution of the HTAPs, a mouse model bearing subcutaneous 4T1 tumor xenografts was established. When the tumor volume was approximately 300 mm^3, the mice were

randomly assigned to different groups ($n = 3$). Then, Taxol, Abraxane or HTAPs were administered (7 mg/kg equivalent to PTX). At 1, 4 and 12 h, the mice were euthanized respectively to collect the tumors, hearts, livers, spleens, lungs and kidneys. After the tissues were homogenized, quantitative analysis of PTX and its prodrug was performed using UPLC−MS/MS.

DiR or DiR-labeled HTAPs were administered (1 mg/kg equivalent to DiR). The mice were euthanized at 1, 4 and 12 h, and the fluorescence intensity of each tissue was measured.

2.17. Antitumor effect

4T1 cells were subcutaneously inoculated into the dorsal flank of female BALB/c mice to obtain the tumor model. Mice were randomly divided into different groups ($n = 5$) once the tumor reached a size of approximately 100 mm^3. The mice were administered saline, Taxol (only at 20 mg/kg due to its toxicity), Abraxane or HTAPs intravenously at doses of equivalent to 20 or 40 mg/kg of PTX. The first three doses were given every other day; a fourth dose was administered time every two days. Tumor volume and body weight were recorded daily. On Day 10, the mice were euthanized and the tumors were excised and weighed. Tumor burden and tumor growth inhibition value were using the following Eqs. (5), (6), and (7):

$$\text{Tumor volume}\left(mm^3\right) = \frac{L \times W \times W}{2} \quad (5)$$

Where L represents the tumor length, and W represents the tumor width.

$$\text{Tumor burden}\,(\%) = \frac{M_t}{M_m} \times 100 \quad (6)$$

Where M_t represents the weight of the tumor (g) and M_m represents the weight of the mouse (g).

$$\text{Tumor growth inhibition value}\,(\%) = \frac{\text{CTV} - \text{TTV}}{\text{CTV}} \times 100\% \quad (7)$$

Where CTV represents the tumor volume of the saline group and TTV represents the tumor volume of the treatment group.

2.18. Safety assessment

During treatment, the body weight of mice was measured daily, the weight change curve was plotted. If the body weight was below 85% of that before administration, the drug should be withheld. If the body weight was below 80% of that before administration, the mice were terminated the experiment.

After the completion of the anti-tumor study, organs such as the heart, liver, spleen, lung, kidney, and tumor from each group were collected for H&E staining. Blood samples were taken for blood routine analysis, and centrifuged to obtain the serum for hepatic and renal function analysis.

2.19. Statistical analysis

All quantitative data are presented as mean ± standard deviation (SD). Statistical analyses were performed using GraphPad Prism 9.5.1 software, including two-tailed Student's *t*-tests and one-way ANOVA. P value < 0.05 was considered as significant. ns means not significant, $*P < 0.05$, $**P < 0.01$, $***P < 0.001$, $****P < 0.0001$. Additional specialized analyses were conducted using: FlowJo (v10.8.1 CL) for flow cytometry data processing, Fiji software for Pearson correlation coefficients, and DAS 2.0 software for pharmacokinetic parameter calculations.

3. Results and discussion

3.1. Design and synthesis of PTX prodrugs

Here, to find out the relationship between the differences in heteroatomic cyclic structures and the properties of prodrug nanoassemblies, we selected three representative cyclic modification chains (named morpholino, cyclohexyl and piperidino, respectively) to conjugate with PTX *via* the disulfide bond. The resulting heterocyclic tertiary amine−PTX prodrugs (HTAP) were designated as PTX−SS−NO, PTX−SS−CC, and PTX−SS−NC, respectively. The detailed synthetic procedure of HTAP was illustrated in Supporting Information Scheme S1. The successfully synthesized PTX−SS and HTAPs were purified, and their molecular structures were confirmed by mass spectrometry (MS) and ^{1}H NMR (Supporting Information Figs. S1−S4). Before conducting the follow-up experiments, the purity of the four prodrugs was assessed by HPLC and found to be above 99% in all cases.

3.2. Self-assembly and stability of HTAPs

To investigate the indispensable role of the heterocyclic tertiary amine in facilitating the self-assembly of prodrugs, the intrinsic self-assembly ability of the prodrugs was initially evaluated. We used a one-step nanoprecipitation method to prepare prodrug nanoassemblies. An organic solution containing prodrugs was added dropwise to a certain proportion of water, followed by the removal of the organic solvent from the mixture[31]. The obtained nanoassemblies were denoted as non-PEGylated HTAPs (non-PEGylated PTX−SS−NO NPs, non-PEGylated PTX−SS−CC NPs and non-PEGylated PTX−SS−NC NPs, respectively). As illustrated in Supporting Information Figs. S5 and S6, three concentrations (0.1, 0.2, and 0.4 mg/mL) of prodrug nanoassemblies were evaluated. Notably, non-PEGylated PTX−SS−NO NPs successfully formed uniform and stable nanoassemblies at all three concentrations. In contrast, PTX−SS−NC failed to form nanoassemblies across all the concentrations, while non-PEGylated PTX−SS−CC NPs were unable to form nanoassemblies at higher concentrations (0.2 or 0.4 mg/mL). Consequently, the order of self-assembly stability for non-PEGylated HTAPs was as follows: non-PEGylated PTX−SS−NO NPs > non-PEGylated PTX−SS−CC NPs > non-PEGylated PTX−SS−NC NPs.

The hydrophobic interactions between prodrug molecules served as the primary driving force for self-assembly[32]. Initially, we calculated the oil-water partition coefficient (Log P values) of HTAP and PTX. As illustrated in Fig. 2A, HTAP exhibited greater hydrophobicity compared to PTX, indicating enhanced intermolecular hydrophobic interactions that facilitated their self-assembly into nanoassemblies. However, if the hydrophobic forces are too strong, they could cause excessive aggregation and precipitation of prodrug molecules, as observed with non-PEGylated PTX−SS−CC NPs and non-PEGylated PTX−SS−NC NPs (Fig. S5). For PTX−SS−NO, the presence of a terminal hydrophilic oxygen atom helped to interact with water molecules, thereby preventing excessive aggregation and maintaining optimal assembly stability. Meanwhile, molecular simulations further demonstrated that PTX−SS−NO maintained

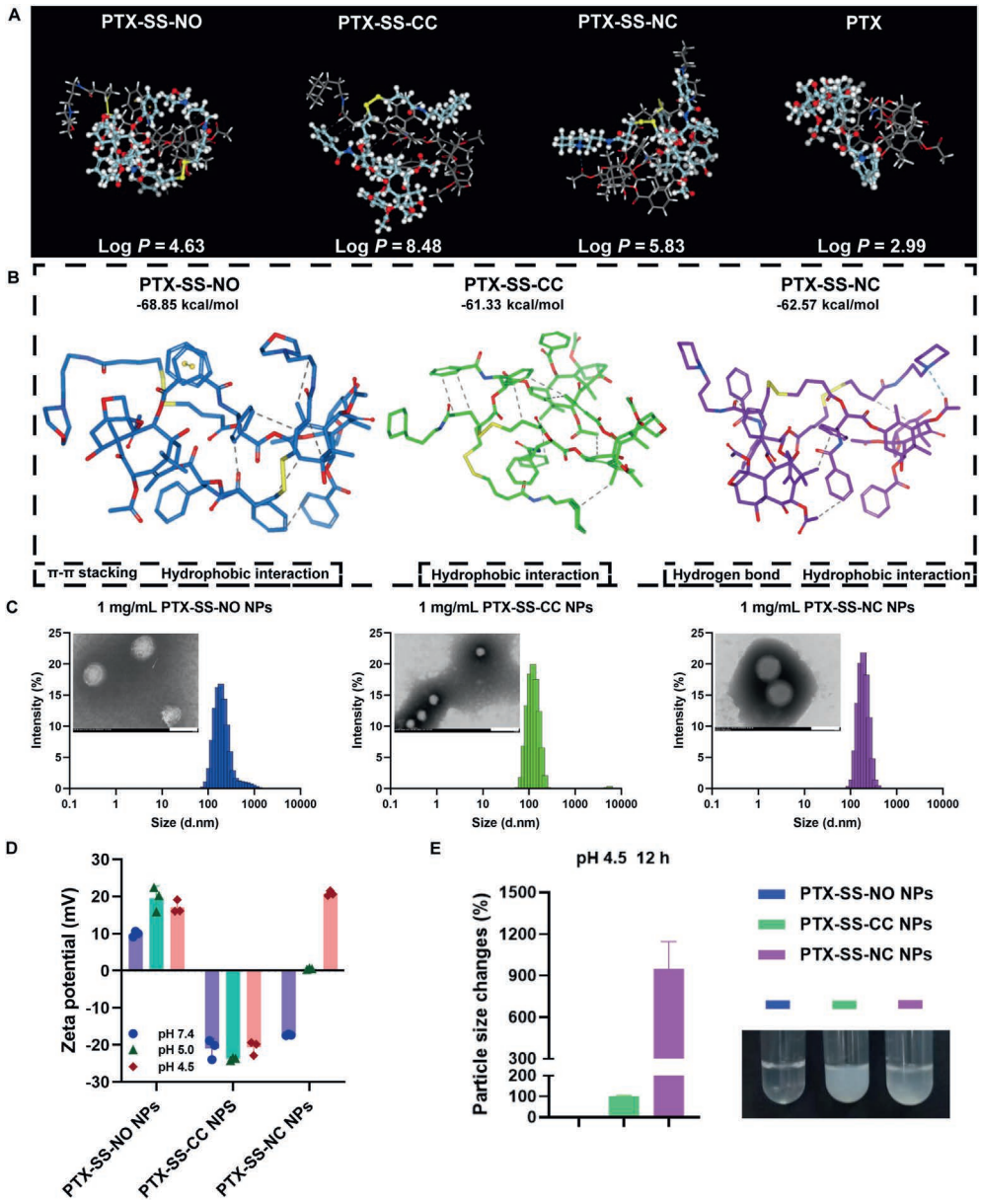

Figure 2 Preparation and characterization of HTAPs. (A) Log *P* values of HTAPs and PTX. (B) Molecular docking conformation and intermolecular forces. (C) TEM images and particle size distribution profiles of HTAPs. Scale bar = 200 nm. (D) Zeta potential change. (E) HTAPs were placed at pH 4.5 for 12 h. Data are presented as mean ± SD (n = 3).

the lowest binding free energy (−68.85 kcal/mol) during the assembly process, confirming its superior stability (Fig. 2B).

In the previous work, we found that the non-PEGylated prodrug nanoassemblies had poor stability in PBS due to their highly hydrophobic surface. In addition, the non-PEGylated prodrug nanoassemblies exhibited an even shorter blood circulation time than that of Taxol due to the poor stability and the highly hydrophobic surface of nanoassemblies, which could be easily phagocytosed by the reticuloendothelial system[33]. However, adding a small amount of PEG can effectively enhance the *in vivo* stability of nanoparticles. PEGylation could facilitate the formation of a hydration layer on nanoassemblies' surface to mitigate protein adsorption and immune recognition, thereby enhancing the circulation time in blood[34−36]. Furthermore, our previous studies demonstrated that the amount of DSPE-PEG_{2k} also affected the *in vitro* and *in vivo* fate of prodrug nanoassemblies, and the prodrug nanoassemblies containing 20% DSPE-PEG_{2k} (*w/w*) showed better stability, higher cellular uptake efficiency, stronger cytotoxic activity, higher AUC (area under the plasma concentration − time curve) and much better antitumor efficacy[37]. Therefore, a 4:1 weight ratio of prodrugs to DSPE-PEG_{2k} was selected as the optimal formulation for this study. We prepared PEGylated nanoassemblies named PTX−SS−NO NPs, PTX−SS−CC NPs, and PTX−SS−NC NPs, respectively. As depicted in Fig. 2C and Supporting Information Table S1, all HTAPs exhibited particle sizes within the range of 100−200 nm and displayed spherical morphology with a drug load of approximately 57%. Among them, PTX−SS−NO NPs possessed positive charge while both PTX−SS−CC NPs and PTX−SS−NC NPs displayed negative charges (approximately −21 mV for PTX−SS−CC NPs and

−17 mV for PTX−SS−NC NPs). We investigated their stability under various conditions. As illustrated in Supporting Information Fig. S7, HTAPs remained stable even after incubation in fetal bovine serum (FBS) for 24 h. Furthermore, there was no significant change in particle size after 30 days of storage at both 4 °C and room temperature. These results indicated that PEG modification can effectively improve the stability of nanoassemblies.

The interior of the lysosome has been demonstrated to possess an acidic environment, characterized by a pH range of approximately 4.5−5.5[38]. We then investigated the alterations of HTAPs after entry into lysosomes. To simulate the acidic environment in lysosomes, we adjusted the pH of nanoassemblies accordingly to observe the change in particle size and appearance. Transitioning from pH 7.4 to pH 4.5 revealed that PTX−SS−NO NPs consistently maintained a positive charge (from 9.9 to 17.1 mV). PTX−SS−CC NPs retained a negative charge throughout. Only PTX−SS−NC NPs underwent a charge inversion from negative (−17.3 mV) to positive (20.8 mV). Following incubation for 12 h, PTX−SS−NO NPs were destroyed and presented a clear and transparent appearance. No significant changes were observed for PTX−SS−CC NPs. However, aggregation and sedimentation occurred with PTX−SS−NC NPs under these conditions (Fig. 2D and E). This phenomenon was attributed to the protonation of the tertiary amine in the cyclic modification module under acidic conditions, leading to the charge of PTX−SS−NC NPs shifting from negative to positive. In contrast, PTX−SS−CC NPs, which lack a tertiary amine, remained unaffected by pH changes. PTX−SS−NO NPs, containing both oxygen and nitrogen atoms with lone pairs of electrons, exhibited a stronger ability to bind with protons. As a result, PTX−SS−NO NPs carried a positive charge even in neutral environments. Under acidic conditions, more protons were attracted to the oxygen and nitrogen atoms, further enhancing the hydrophilic interactions. Consequently, the hydrophilic force gradually surpassed the hydrophobic force, leading to the disintegration of the PTX−SS−NO NPs.

3.3. *In vitro drug release of the HTAPs*

Subsequently, we investigated the drug release behavior of HTAPs *in vitro* (Fig. 3A). In the blank medium, only a negligible amount of PTX was released (Fig. 3B), which could help minimize premature drug release into the bloodstream. HTAPs exhibited a slower release rate at lower pH, indicating the need for HTAPs to escape the acidic lysosomal environment for effective release. As

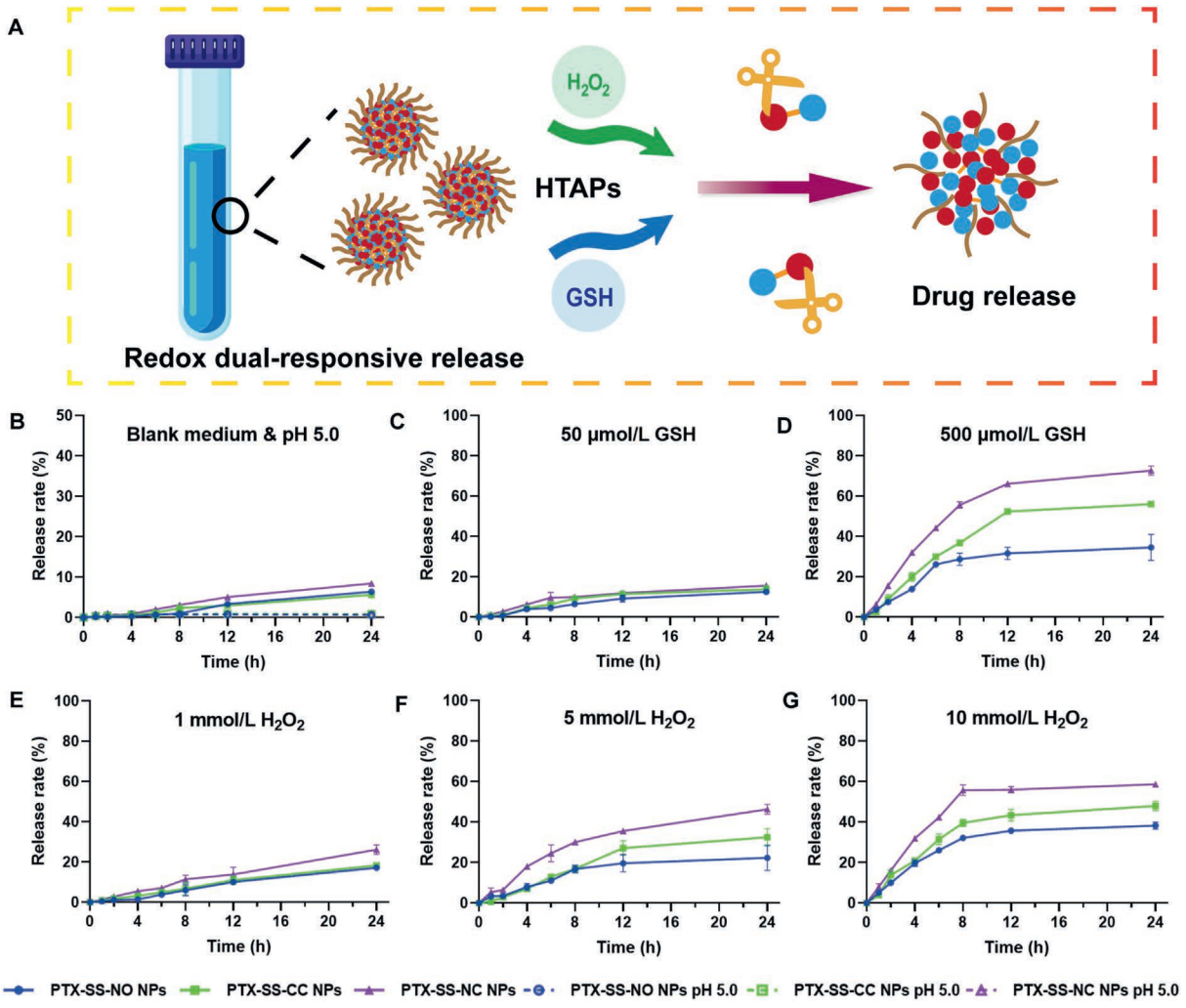

Figure 3 Schematic illustrates the release of HTAPs and stimulus-responsive drug release profiles. (A) Schematic illustrates the release of HTAPs. (B) *In vitro* release of the HTAPs in blank medium and at pH 5.0 medium. (C, D) Reductive release of HTAPs at 50 and 500 μmol/L GSH, respectively. (E−G) Oxidative release of HTAPs at 1, 5, and 10 mmol/L H_2O_2, respectively. Data are presented as mean ± SD (n = 3).

tumor cells exhibit elevated levels of ROS and GSH in the cytoplasm compared to normal cells, we further investigated the drug release profile of HTAPs under conditions involving H_2O_2 and GSH. As illustrated in Fig. 3C and D, at a concentration of 50 μmol/L GSH, the released PTX from HTAPs remained below 20%. Upon increasing GSH concentration to 500 μmol/L, PTX−SS−NC NPs demonstrated higher levels of released PTX compared to PTX−SS−CC NPs and PTX−SS−NO NPs. We then tested the drug release under oxidative conditions. When the concentration of H_2O_2 was 1 mmol/L, the PTX release from HTAPs was approximately 20% (Fig. 3E). As the H_2O_2 concentration increased from 1 to 10 mmol/L, PTX released gradually elevated, following a trend similar to that observed with GSH: PTX−SS−NC NPs > PTX−SS−CC NPs > PTX−SS−NO NPs (Fig. 3F and G). These findings aligned with the results of self-assembly stability, which indicated that the enhanced stability of HTAPs contributed to a slower release rate of PTX.

3.4. *In vitro antitumor activity of the HTAPs*

Cytotoxicity assays serve as an intuitive approach to evaluate the efficacy of prodrug nanoassemblies[39]. Thus, we assessed the toxicity of HTAPs and HTAP aq against various tumor cells, including 4T1 cells, B16-F10 cells, and A549 cells. As depicted in

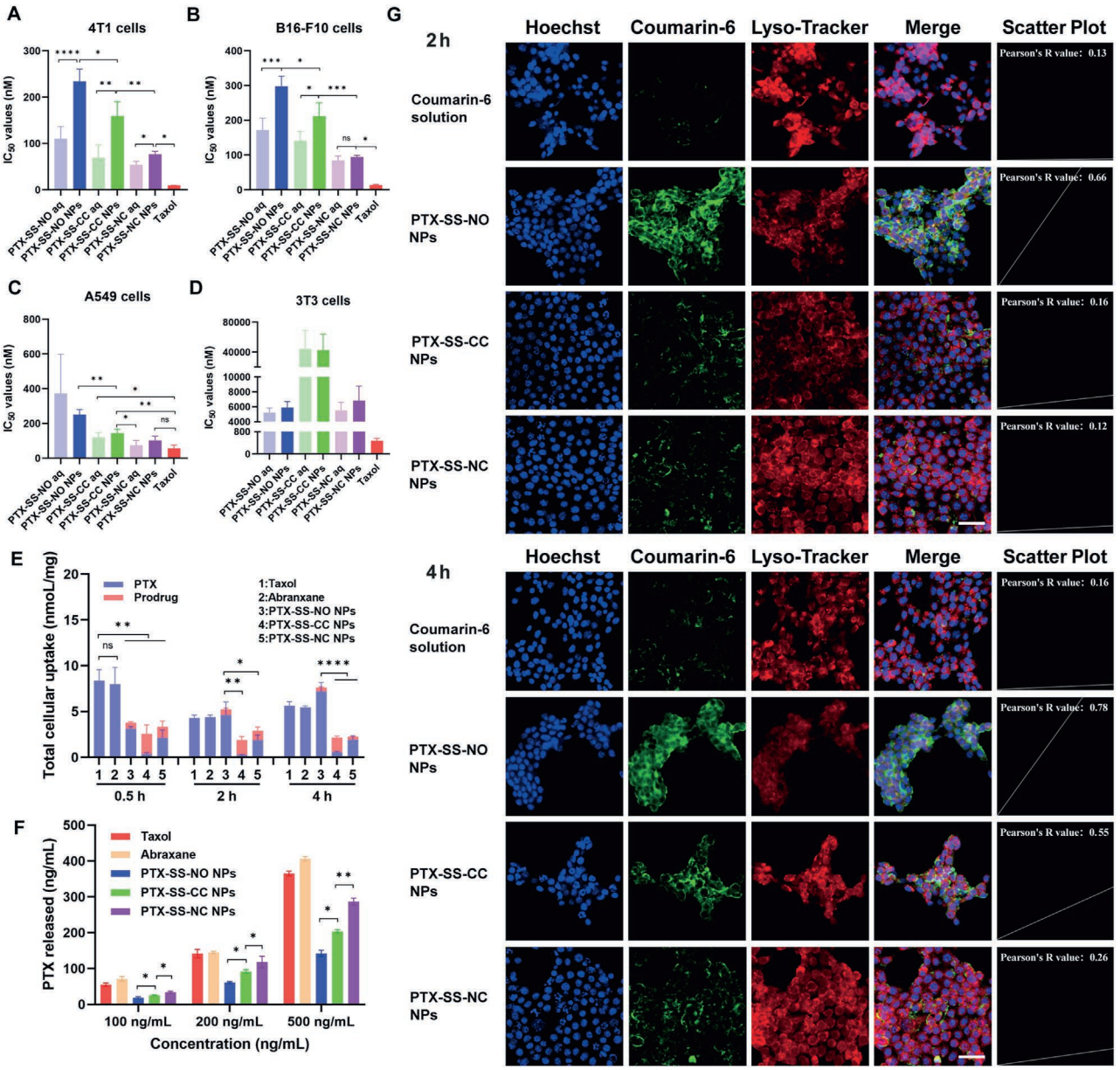

Figure 4 *In vitro* antitumor activity. (A−D) The IC_{50} values of 4T1 cells, B16-F10 cells, A549 cells, and 3T3 cells. (E) Cellular uptake was determined by UPLC−MS/MS. (F) Free PTX released from Taxol, Abraxane and HTAPs after incubation with 4T1 cells for 48 h. (G) CLSM images showing lysosomal colocalization at 2 and 4 h. Scale bar = 50 μm. Data are presented as mean ± SD (n = 3). Statistical results were analyzed by one-way analysis of variance (ANOVA) and student's t-test (two-tailed), ns, not significant, *$P < 0.05$, **$P < 0.01$, ***$P < 0.001$, ****$P < 0.0001$ *vs.* indicated.

Fig. 4A−C, Taxol exhibited the lowest IC_{50} value and the strongest cytotoxic effects across all the tumor cell types. Its potency arose from its ability to act directly on tubulin, without the rate-limiting process of drug release. Among the HTAPs, PTX−SS−NC NPs exhibited the highest cytotoxicity, followed by PTX−SS−CC NPs, while PTX−SS−NO NPs showed relatively lower cytotoxicity. Cytotoxicity rankings mirrored the *in vitro* redox release rate. Interestingly, HTAP aq displayed slightly stronger cytotoxicity than the HTAPs, probably attributed to their different cellular uptake mechanisms. HTAPs entered into cells through energy-dependent endocytosis, requiring passage through lysosomes, whereas HTAP aq diffused directly across the membrane into the cytoplasm.

In addition, evaluating the cytotoxicity of HTAPs and HTAP aq on normal cells was a crucial parameter to assess their safety. The selectivity index (SI) served as an important indicator to assess the selectivity between tumor cells and normal cells. We further investigated the toxicity of HTAPs and HTAP aq on 3T3 normal cells (Fig. 4D). Taxol exhibited the highest cytotoxicity due to its non-selective characteristics. According to Supporting Information Table S2, HTAPs, PTX−SS−CC aq, and PTX−SS−NC aq demonstrated significantly higher SI values compared to Taxol. However, in several tumor cell lines, the SI values of PTX−SS−NO NPs and PTX−SS−NO aq were lower than those of Taxol, indicating poor selectivity issues associated with a high positive charge of PTX−SS−NO.

3.5. Cellular uptake and lysosome escape

We then examined cellular uptake of HTAPs using qualitative and quantitative methods, respectively. PTX−SS−NO NPs exhibited a much stronger fluorescence intensity than PTX−SS−NC NPs and PTX−SS−CC NPs (Supporting Information Fig. S8). This could be attributed to the strong binding affinity between positively charged PTX−SS−NO NPs and negatively charged tumor cell membrane surface, which enhanced cellular uptake. Furthermore, consistent with the findings from fluorescence analysis, the quantitative assay also demonstrated that PTX−SS−NO NPs exhibited greater cellular uptake than PTX−SS−CC NPs and PTX−SS−NC NPs (Fig. 4E). However, this significant cellular uptake did not result in a high cytotoxic effect of the nanoassemblies, which may be related to strong lysosomal entrapment.

Subsequently, we employed chlorpromazine (a clathrin-mediated endocytosis inhibitor), quercetin (a non-clathrin/non-caveolae-mediated endocytosis inhibitor), indomethacin (a caveolae-mediated endocytosis inhibitor), and colchicine (a macropinocytosis inhibitor) to investigate the cellular uptake pathways of HTAPs. The results indicated that PTX−SS−NO NPs primarily entered cells *via* non-clathrin/non-caveolae-mediated endocytosis; whereas PTX−SS−CC NPs and PTX−SS−NC NPs entered cells mainly through non-clathrin/non-caveolae, caveolae, and macropinocytosis-mediated endocytosis (Supporting Information Fig. S9).

HTAPs were typically transported to lysosomes, which are membrane-bound and low-pH compartments containing various digestive enzymes or hydrolases. In addition, *in vitro* release experiments also demonstrated that low-pH conditions decreased the release of PTX (Fig. 3A). As mentioned above, the presence of tertiary amine structure altered the physicochemical properties of PTX−SS−NO NPs and PTX−SS−NC NPs under acidic conditions (Fig. 2E). Although PTX−SS−NO NPs demonstrated the highest cellular uptake among the HTAPs, their lipophilicity decreased after protonation in lysosomes, leading to a reduction in membrane permeability. Additionally, positively charged PTX−SS−NO NPs exhibited higher affinity towards negatively charged lysosome membranes. In the hemolysis experiment under the condition of pH 4.5, the positively charged PTX−SS−NO NPs caused the leakage of a small amount of hemoglobin in the red blood cells through membrane electrostatic adsorption (Supporting Information Fig. S10). But intracellular release experiments have shown minimal PTX was released from PTX−SS−NO NPs at 48 h (Fig. 4F). Consequently, most PTX−SS−NO NPs were trapped within lysosomes, preventing interaction with ROS or GSH mainly in the cytoplasm. On the other hand, PTX−SS−NC NPs absorbed a large number of protons, and the charge switches from negative to positive (Fig. 2D). Through membrane electrostatic adsorption and osmotic pressure imbalance, it causes higher hemolysis percentage (Fig. S10). That is to say, moderate protonation of PTX−SS−NC NPs in lysosomes induced a proton sponge effect, resulting in lysosomal rupture and drug release (Fig. 4F). This escape mechanism facilitated substantial drug delivery into the cytoplasm for therapeutic action.

To further investigate the disparity in lysosomal escape efficiency among HTAPs, we employed Pearson correlation coefficient to assess the co-localization of HTAPs and lysosomes (Fig. 4G and Supporting Information Fig. S11). The Pearson correlation coefficient between PTX−SS−NO NPs and lysosomes exhibited the highest value, indicating that a majority of PTX−SS−NO NPs were restricted in lysosomes. Therefore, minimal PTX was released from PTX−SS−NO NPs into the cytoplasm. The Pearson correlation coefficient for PTX−SS−CC NPs displayed an increasing trend, suggesting ongoing cellular uptake. PTX−SS−NC NPs exhibited a slower increase in Pearson correlation coefficient compared to others with consistently lower values at all time points. These findings indicated that PTX−SS−NC NPs possessed a superior proton sponge effect and were more prone to escaping from lysosomes. Collectively, cellular uptake as well as intracellular release and lysosome co-localization studies corroborated cytotoxicity results: PTX−SS−NC NPs demonstrated optimal efficacy due to its superior ability to escape from lysosomes, resulting in increased release of PTX at target sites. Conversely, despite higher cellular uptake, PTX−SS−NO NPs showed poor release leading to diminished cytotoxicity effects.

3.6. Pharmacokinetic and biodistribution

Before the pharmacokinetic study, hemolysis tests were conducted on Taxol and HTAPs. As depicted in Supporting Information Fig. S12, when reaching a concentration of 100 μg/mL, the hemolysis percentage of PTX−SS−NO NPs was higher than 5%, indicating notable toxicity due to their positive charge. PTX−SS−CC NPs and PTX−SS−NC NPs showed similar surface properties, resulting in comparable hemolysis percentages. However, Taxol exhibited a high hemolysis percentage of up to 30%, raising serious safety concerns. The dose was therefore reduced to 6 mg/kg. In Fig. 5A−C and Supporting Information Table S3, both Taxol and Abraxane were rapidly cleared with low half-life ($t_{1/2}$). Conversely, PTX−SS−CC NPs and PTX−SS−NC NPs demonstrated significantly increased $t_{1/2}$ values and C_{max} levels. Moreover, $AUC_{0-24\ h}$ was enhanced by 3−4 times for PTX−SS−CC NPs. However, the drug concentration of PTX−SS−NO NPs remained consistently low, since highly positively charged nanoassemblies were easily recognized and phagocytosed by mononuclear phagocytes[40].

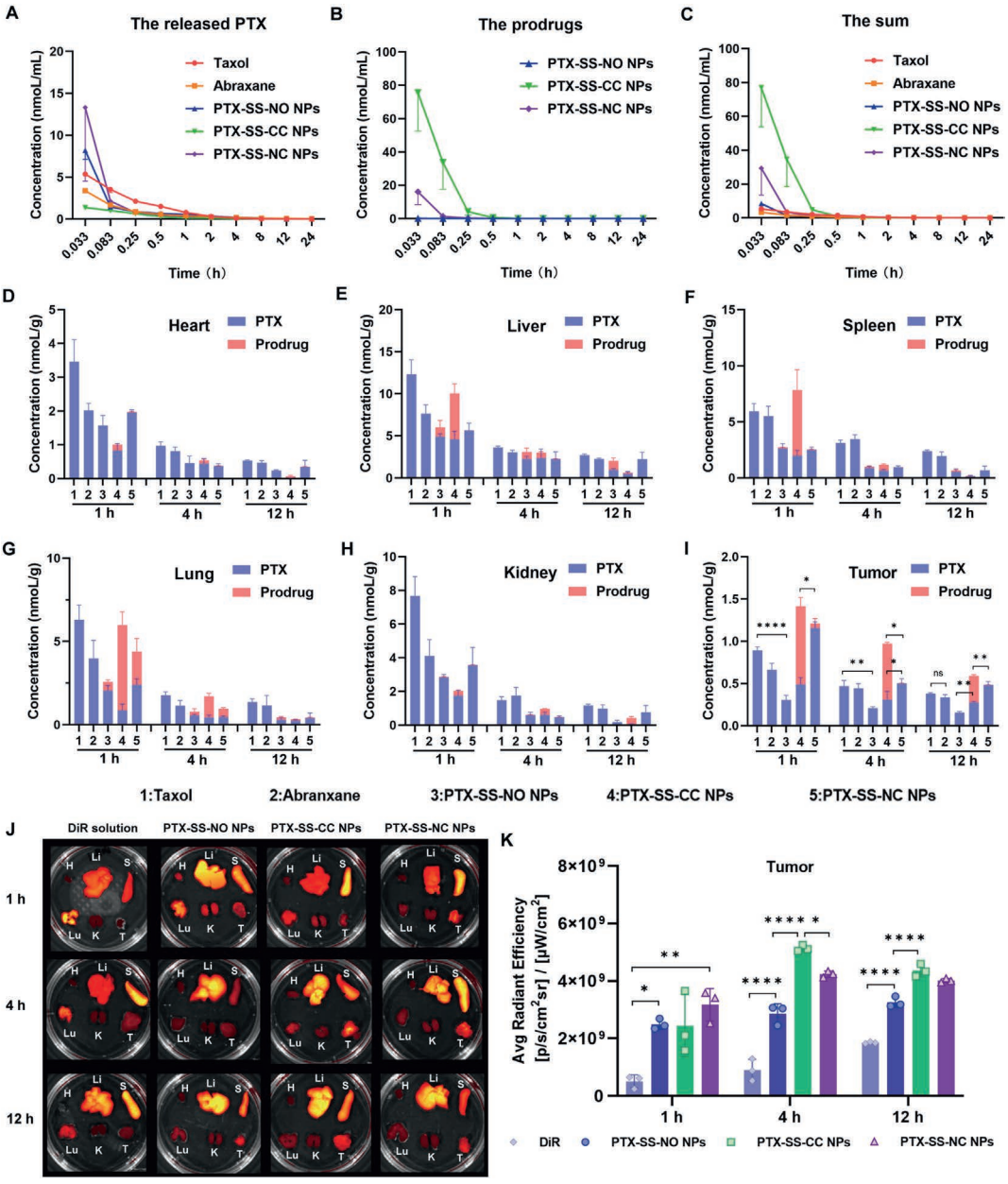

Figure 5 Pharmacokinetics and biodistribution studies. Molar concentration−time curves of (A) the released PTX, (B) the prodrug and (C) the sum of prodrugs and the released PTX. (D) Heart, (E) liver, (F) spleen, (G) lung, (H) kidney, and (I) tumor accumulation of Taxol, Abraxane and the HTAPs. (J) Fluorescent images of DiR-labeled HTAPs in main organs and tumors at 1, 4 and 12 h. (K) Quantitative results of tumor accumulation. Data are presented as mean ± SD ($n = 3$). Statistical results were analyzed with one-way analysis of variance (ANOVA) and student's *t*-test (two-tailed), ns, not significant, $^{*}P < 0.05$, $^{**}P < 0.01$, $^{****}P < 0.0001$ *vs*. indicated.

The final therapeutic efficacy of the drug was affected by the distribution of HTAPs, particularly at the tumor site. Using 4T1 tumor-bearing BALB/c mice as a model, we employed UPLC−MS/MS combined with fluorescence labeling to simultaneously investigate the distribution of the prodrug and PTX *in vivo*. As shown in Fig. 5D−I, Taxol and Abraxane exhibited rapid tissue distribution and were quickly cleared from the system. PTX−SS−NC NPs showed excellent accumulation at the tumor site, and almost all PTX was released due to their superior lysosomal escape capability and strong redox sensitivity. PTX−SS−CC NPs exhibited a remarkably slower release rate of PTX in tumors, potentially limiting their therapeutic efficacy. In contrast, the tumor accumulation of PTX−SS−NO NPs was minimal, consistent with the pharmacokinetic results. The findings from fluorescence analysis aligned with those observed in UPLC−MS/MS (Fig. 5J and K). PTX−SS−NC NPs exhibited strong fluorescence intensity and substantial accumulation at the tumor site, whereas PTX−SS−NO NPs showed the least distribution at the tumor site.

3.7. *Antitumor effect and biosafety*

To investigate the impact of HTAPs on tumor progression *in vivo*, we assessed the antitumor efficacy of HTAPs using two dosing regimens: 20 and 40 mg/kg in the 4T1 tumor model (Fig. 6A and

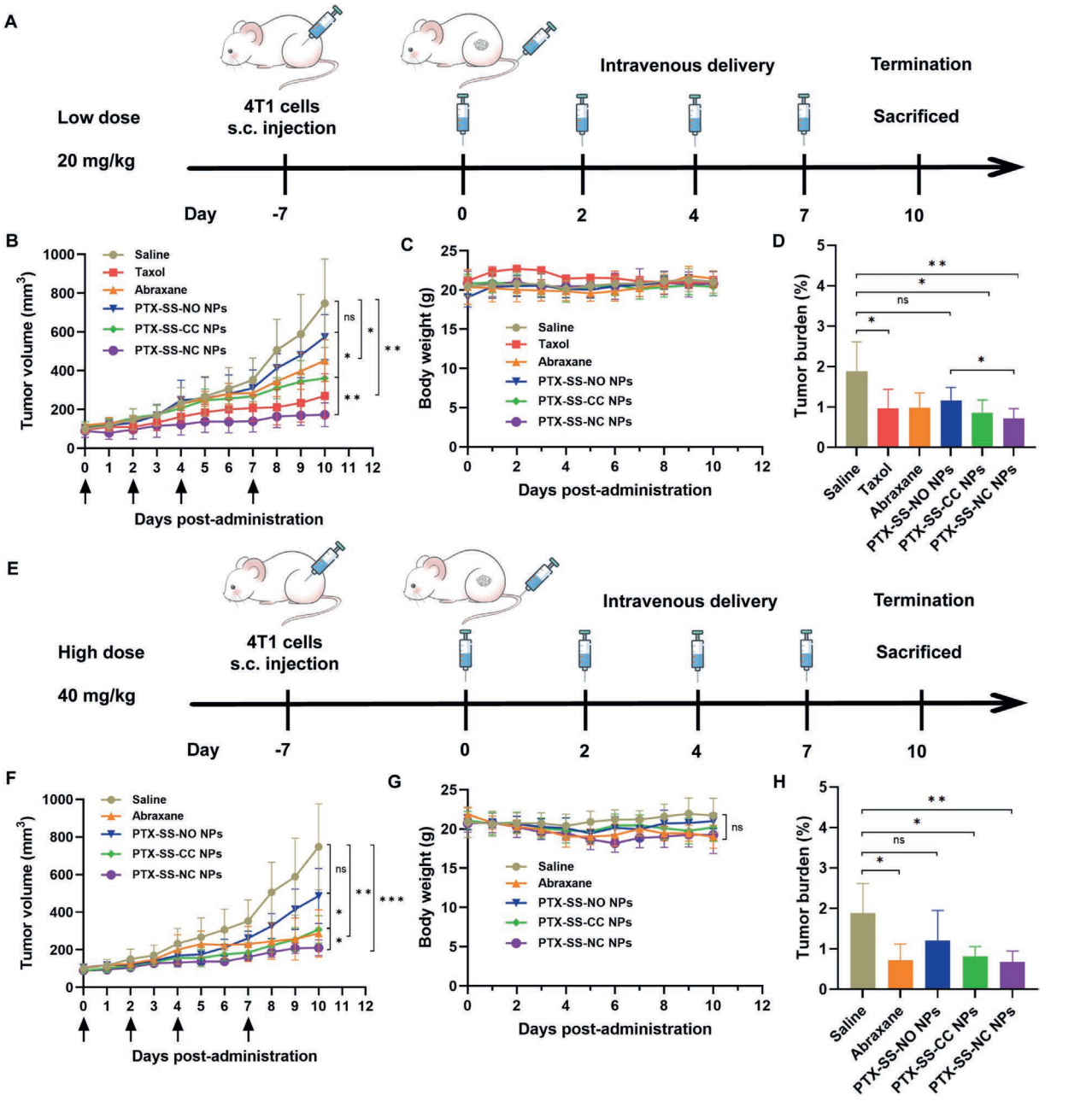

Figure 6 Antitumor study. (A) Schematic representation of low-dose treatment. (B) Tumor growth curves, (C) Body weight curves, and (D) Tumor burden after the treatment of 20 mg/kg HTAPs, Taxol and Abraxane. (E) Schematic representation of high-dose treatment. (F) Tumor growth curves, (G) Body weight curves, and (H) Tumor burden after the treatment of 40 mg/kg HTAPs and Abraxane. Data are presented as mean ± SD ($n = 5$). Statistical differences were analyzed with one-way analysis of variance (ANOVA) and student's *t*-test (two-tailed), ns, not significant, $^{*}P < 0.05$, $^{**}P < 0.01$, $^{***}P < 0.001$ *vs.* indicated.

E). At a lower dose of 20 mg/kg, PTX−SS−NC NPs exhibited optimal inhibition of tumor growth due to efficient accumulation and release of PTX at tumor sites (Fig. 6B and Supporting Information Fig. S13A), which was consistent with the findings from biodistribution analysis. Furthermore, safety evaluation did not reveal any abnormalities associated with PTX−SS−NC NPs (Fig. 6C and Supporting Information Fig. S14A, B and E). In contrast, the Taxol group showed abnormally reduced WBC counts (Fig. S14A). Besides, PTX−SS−CC NPs displayed slightly less effectiveness in inhibiting tumor growth due to slower drug release (Fig. 6B and D). PTX−SS−NO NPs exhibited poor antitumor effects as they were easily eliminated from the body (Fig. 6B and D).

Next, the dosage was escalated to 40 mg/kg. However, Taxol at this dose led to rapid death of the mice. Consequently, the Taxol group was excluded from further analysis at this dosage level. Despite Abraxane exerting a strong antitumor effect, it significantly reduced WBC and PLT counts and increased AST levels, indicating poor safety at high dose (Fig. 6F, Fig. S14B−S14D and S14F). In contrast, PTX−SS−NC NPs still showed the best antitumor efficacy. However, the 4T1 model used in our antitumor study is a type of triple-negative breast cancer. Besides, the

microenvironment of malignant tumors such as triple-negative breast cancer is complex, and the growth and metastasis of cancer cells are rapid, which poses a challenge for the complete cure of cancer with drugs. All these may have led to the result that increasing the dosage of PTX−SS−NC NPs did not significantly improve the therapeutic effect. Notably, PTX−SS−NC NPs did not exhibit any adverse effects on body weight (Fig. 6F−H and Fig. S13B), hematological parameters (Fig. S14B and S14D), hepatorenal function (Fig. S14F), or histopathology findings (Supporting Information Fig. S15). These observations collectively validated both the safety and efficacy of PTX−SS−NC NPs.

4. Conclusions

In this study, we designed PTX prodrugs using heterocyclic tertiary amine as modification modules. The heterocyclic structure influenced the intermolecular forces of prodrugs, thereby altering the stability and drug release rate of HTAPs. The greater the assembly stability, the slower the stimulus-responsive release rate of HTAPs, so the drug release rate was: PTX−SS−NO NPs < PTX−SS−CC NPs < PTX−SS−NC NPs. The presence of the tertiary amine structure led to different behaviors of HTAPs within cellular lysosomes, including lysosomal escape or entrapment. PTX−SS−NO NPs had the lowest cytotoxicity owing to slow drug release and lysosomal sequestration, although they had the highest cellular uptake. In contrast, PTX−SS−NC NPs demonstrated the fastest release rate and lysosomal escape, resulting in the highest cytotoxicity. In addition, PTX−SS−NO NPs were rapidly cleared from the system resulting in the worst pharmacokinetic properties, thereby limiting efficacy. Although PTX−SS−CC NPs exhibited prolonged circulation time, their drug release rate was slower. PTX−SS−NC NPs had excellent tumor accumulation, coupled with superior cellular delivery and release properties, which achieved the most effective antitumor efficacy. Notably, PTX−SS−NC NPs demonstrated favorable safety due to intelligent drug release. Overall, employing heterocyclic tertiary amine structures as modification modules effectively circumvents lysosomal entrapment of prodrug nanoassemblies.

Acknowledgments

This work was financially supported by National Key R&D Program of China (No. 2022YFE0111600), Liaoning Revitalization Talents Program (No. No XLYC22202019 and XLYC2203083, China), Youth Innovation Team of Liaoning Province Department of Education (No. LJ222410163049. China), and Key Research and Development Program of Liaoning Province (2024JH2/102500061, China).

Author contributions

Cong Luo, Bingjun Sun, and Jin Sun designed the research. Mingyang Han and Hezhen Xu carried out the experiments and performed data analysis. Jun Yuan, Wenxiao Li, Hao Zhang, Hongkai Fang, Zhiyu Kuang, Yuanhao Yu, Danping Wang and Zhenzhen Zhao participated part of the experiments. All of the authors have read and approved the final manuscript.

Conflicts of interest

The authors declare no conflicts of interest.

Appendix A. Supporting information

Supporting information to this article can be found online at https://doi.org/10.1016/j.apsb.2026.01.017.

References

1. Hellmann MD, Li BT, Chaft JE, Kris MG. Chemotherapy remains an essential element of personalized care for persons with lung cancers. *Ann Oncol* 2016;**27**:1829−35.
2. Chen Q, Liu GX, Liu S, Su HY, Wang Y, Li JY, et al. Remodeling the tumor microenvironment with emerging nanotherapeutics. *Trends Pharmacol Sci* 2018;**39**:59−74.
3. Howat S, Park B, Oh IS, Jin Y-W, Lee E-K, Loake GJ. Paclitaxel: biosynthesis, production and future prospects. *N Biotech* 2014;**31**:242−5.
4. Wang LQ. Preparation and *in vitro* evaluation of an acidic environment-responsive liposome for paclitaxel tumor targeting. *Asian J Pharm Sci* 2017;**12**:470−7.
5. Wang HB, Cheng G, Du Y, Ye L, Chen WZ, Zhang L, et al. Hypersensitivity reaction studies of a polyethoxylated Castor oil-free, liposome-based alternative paclitaxel formulation. *Mol Med Rep* 2013;**7**:947−52.
6. Zong Y, Wu JY, Shen KW. Nanoparticle albumin-bound paclitaxel as neoadjuvant chemotherapy of breast cancer: a systematic review and meta-analysis. *Oncotarget* 2017;**8**:17360−72.
7. Li GT, Sun BJ, Li YQ, Luo C, He ZG, Sun J. Small-molecule prodrug nanoassemblies: an emerging nanoplatform for anticancer drug delivery. *Small* 2021;**17**:e2101460.
8. Luo C, Sun BJ, Wang C, Zhang XB, Chen Y, Chen Q, et al. Self-facilitated ROS-responsive nanoassembly of heterotypic dimer for synergistic chemo-photodynamic therapy. *J Control Release* 2019;**302**:79−89.
9. Wang FS, Fan YL, Liu Y, Lou XX, Sutrisno L, Peng SJ, et al. Oxygen-carrying semiconducting polymer nanoprodrugs induce sono-pyroptosis for deep-tissue tumor treatment. *Exploration* 2024;**4**:20230100.
10. Guo CQ, Lin L, Wang YH, Jing J, Gong QY, Luo K. Nano drug delivery systems for advanced immune checkpoint blockade therapy. *Theranostics* 2025;**15**:5440−80.
11. Li LX, Liu T, Zuo SY, Li YQ, Zhao EW, Lu Q, et al. Satellite-type sulfur atom distribution in trithiocarbonate bond-bridged dimeric prodrug nanoassemblies: achieving both stability and activatability. *Adv Mater* 2024;**36**:e2310633.
12. Li GT, Jin QH, Xia FL, Fu SW, Zhang XB, Xiao HY, et al. Smart stimuli-responsive carrier-free nanoassembly of SN38 prodrug as efficient chemotherapeutic nanomedicine. *Acta Mater Medica* 2023;**2**:54−63.
13. Wang X, Li LX, Wang DP, Zuo SY, Liu T, Dong FD, et al. Minor change in the length of carbon chain has a great influence on the antitumor effect of paclitaxel-fatty alcohol prodrug nanoassemblies: small roles, big impacts. *Nano Res* 2021;**15**:1−9.
14. Lei L, Song YJ, Yang LY, Wang YZ, Xia X, Zhang YW, et al. Triethylamine-mediated protonation−deprotonation unlocks dual-drug self assembly to suppress breast cancer progression and metastasis. *Proc Natl Acad Sci* 2025;**122**:e2416796122.
15. Sun BJ, Luo C, Cui WP, Sun J, He ZG. Chemotherapy agent-unsaturated fatty acid prodrugs and prodrug-nanoplatforms for cancer chemotherapy. *J Control Release* 2017;**264**:145−59.
16. Wang S, Liu T, Huang YT, Du CY, Wang DP, Wang XY, et al. The effect of lengths of branched-chain fatty alcohols on the efficacy and safety of docetaxel-prodrug nanoassemblies. *Acta Pharm Sin B* 2024;**14**:1400−11.
17. Xu HZ, Zuo SY, Wang DP, Zhang Y, Li WX, Li LX, et al. Cabazitaxel prodrug nanoassemblies with branched chain modifications: narrowing the gap between efficacy and safety. *J Control Release* 2023;**360**:784−95.
18. Zang WF, Sun YX, Zhang JY, Hao YZ, Jin QH, Xiao HY, et al. Two-tailed modification module tuned steric-hindrance effect enabling high

therapeutic efficacy of paclitaxel prodrug nanoassemblies. *Chin Chem Lett* 2025;**36**:110230.
19. Lou XY, Zhang D, Ling H, He ZG, Sun J, Sun MC, et al. Pure redox-sensitive paclitaxel−maleimide prodrug nanoparticles: endogenous albumin-induced size switching and improved antitumor efficiency. *Acta Pharm Sin B* 2021;**11**:2048−58.
20. Yang YX, Sun BJ, Zuo SY, Li XM, Zhou S, Li LX, et al. Trisulfide bond−mediated doxorubicin dimeric prodrug nanoassemblies with high drug loading, high self-assembly stability, and high tumor selectivity. *Sci Adv* 2020;**6**:eabc1725.
21. Qian C, Zhang Y, Chen XY, Zhu CY, Dong XL, Chen WW, et al. Nanomedicine-encouraged cellular autophagy promoters favor liver fibrosis progression reversal. *View* 2024;**5**:20240003.
22. Saftig P, Sandhoff K. Killing from the inside. *Nature* 2013;**502**:312−3.
23. Sun F, Ning SP, Fan XY, Wang X, Lin ZQ, Zhao J, et al. Engineered cytomembrane nanovesicles trigger *in situ* storm of engineered extracellular vesicles for cascade tumor penetration and immune microenvironment remodeling. *Nano Today* 2025;**61**:102604.
24. Yuan GP, Li MH, Zhang YF, Dong QY, Shao SQ, Zhou ZX, et al. Modulating intracellular dynamics for optimized intracellular release and transcytosis equilibrium. *Adv Mater* 2024;**36**:e2400425.
25. He W, Xing XY, Wang XL, Wu D, Wu W, Guo JL, et al. Nanocarrier-mediated cytosolic delivery of biopharmaceuticals. *Adv Funct Mater* 2020;**30**:1910566.
26. Luo M, Wang H, Wang ZH, Cai HC, Lu ZG, Li Y, et al. A STING-activating nanovaccine for cancer immunotherapy. *Nat Nanotechnol* 2017;**12**:648−54.
27. Liu S, Cheng Q, Wei T, Yu XL, Johnson LT, Farbiak L, et al. Membrane-destabilizing ionizable phospholipids for organ-selective mRNA delivery and CRISPR-Cas gene editing. *Nat Mater* 2021;**20**:701−10.
28. Mei H, Cai SS, Huang D, Gao HL, Cao J, He B. Carrier-free nanodrugs with efficient drug delivery and release for cancer therapy: from intrinsic physicochemical properties to external modification. *Bioact Mater* 2021;**8**:220−40.
29. Zhang H, Liu T, Sun YT, Wang S, Wang WJ, Kuang ZY, et al. Carbon-spaced tandem-disulfide bond bridge design addresses limitations of homodimer prodrug nanoassemblies: enhancing both stability and activatability. *J Am Chem Soc* 2024;**146**:22675−88.
30. Liu T, Li LX, Wang S, Dong FD, Zuo SY, Song JX, et al. Hybrid chalcogen bonds in prodrug nanoassemblies provides dual redox-responsivity in the tumor microenvironment. *Nat Commun* 2022;**13**:7228.
31. Su H, Koo JM, Cui HG. One-component nanomedicine. *J Control Release* 2015;**219**:383−95.
32. Zhang BW, Liu WY, Liu JR, Huang ML, Li YQ, Zhao EW, et al. Rational engineering of cholesterol-modified prodrug nanoassemblies for improving the tumor selectivity and safety of mitoxantrone. *Fundam Res* 2024. Available from: https://doi.org/10.1016/j.fmre.2024.06.006.
33. Luo C, Sun J, Liu D, Sun B, Miao L, Musetti S, et al. Self-assembled redox dual-responsive prodrug-nanosystem formed by single thioether-bridged paclitaxel-fatty acid conjugate for cancer chemotherapy. *Nano Lett* 2016;**16**:5401−8.
34. Li Y, Tong F, Wang YF, Wang J, Wu MQ, Li HM, et al. *In situ* tumor vaccine with optimized nanoadjuvants and lymph node targeting capacity to treat ovarian cancer and metastases. *Acta Pharm Sin B* 2024;**14**:4102−17.
35. Li YK, Shen XD, Ding HT, Zhang YX, Pan DY, Su LP, et al. Dendritic nanomedicine enhances chemo-immunotherapy by disturbing metabolism of cancer-associated fibroblasts for deep penetration and activating function of immune cells. *Acta Pharm Sin B* 2024;**14**:3680−96.
36. Li YK, Wu YH, Fang ZX, Zhang YX, Ding HT, Ren L, et al. Dendritic nanomedicine with boronate bonds for augmented chemo-immunotherapy *via* synergistic modulation of tumor immune microenvironment. *Adv Mater* 2024;**36**:e2307263.
37. Li YQ, Li LX, Jin QH, Liu T, Sun J, Wang YJ, et al. Impact of the amount of PEG on prodrug nanoassemblies for efficient cancer therapy. *Asian J Pharm Sci* 2022;**17**:241−52.
38. Lou XD, Zhang MS, Zhao ZJ, Min XH, Hakeem A, Huang FJ, et al. A photostable AIE fluorogen for lysosome-targetable imaging of living cells. *J Mater Chem B* 2016;**4**:5412−7.
39. Gao YL, Zuo SY, Li LX, Liu T, Dong FD, Wang X, et al. The length of disulfide bond-containing linkages impacts the oral absorption and antitumor activity of paclitaxel prodrug-loaded nanoemulsions. *Nanoscale* 2021;**13**:10536−43.
40. Kamaly N, He JC, Ausiello DA, Farokhzad OC. Nanomedicines for renal disease: current status and future applications. *Nat Rev Nephrol* 2016;**12**:738−53.